A New 3D Compositional Model for Hydraulic Fracturing With Energized Fluids

Lionel H. Ribeiro and **Mukul M. Sharma,** University of Texas at Austin

Summary

While several 3D fracturing models exist for incompressible water-based fluids, none are able to capture the thermal and compositional effects that are important when using energized fluids such as CO_2, N_2, LPG, and foams. This paper introduces a new 3D, compositional, non-isothermal fracturing model. The new model predicts changes in temperature and fluid density. These changes are treated on a firm theoretical basis by using an energy-balance equation and an equation of state, both in the fracture and in the wellbore. The model is capable of handling any multicomponent mixture of fluids and chemicals. Changes in phase behavior with temperature, pressure, and composition can be modeled.

A new simulator has been developed based on the compositional model presented in this paper. The simulator is validated for traditional fluid formulations against known analytical solutions and against a well-established commercial fracturing simulator. Results from the new simulator are then presented for energized fluids such as CO_2 and LPG. In particular, the compositional model shows how fluid expansion and viscosity reduction impact fracture growth. These effects are not captured by traditional fracturing simulators. The compositional tool is specifically suited for fracture design in formations in which energized fluids constitute a viable alternative to traditional fracturing fluids.

Introduction

Limitations of Conventional Water-Fracture Treatments. In many unconventional reservoirs, gas wells do not perform up to potential following water-based fracturing treatments. The suboptimal fracture productivity can be attributed to many factors, such as low reservoir pressure, limited fracture length, poor proppant placement, and low proppant conductivity. Numerous mechanisms have been identified as detrimental to fracture conductivity: (1) water blocking, (2) gel damage, (3) proppant settling, (4) proppant embedment, (5) fines plugging, and (6) clay swelling. The extent of these mechanisms depends on the nature of the interactions between the reservoir rock and the injected fracturing fluid. In some reservoirs, the invasion of water severely damages the reservoir rock and alters fluid saturation, thereby impeding hydrocarbon production.

Operators can also consider alternatives to water treatments because the water supply is limited. Massive slickwater fracturing campaigns require large quantities of water, which may not be readily available either because the water supply is limited; the water quality is not compatible with the desired chemistry (friction reducers, emulsifiers, gelling agent, etc.); or some legislation limits water usage. These factors have prompted the industry to consider waterless fracturing treatments as viable alternatives to water-based fluids. "Water-based fluids" refer here to any single-phase, incompressible, water-based fluids (slickwater, linear gels, and crosslinked gels).

Many alternative fluid formulations exist, and the reader may refer to the summary compiled by Gupta (2011) for a more exhaustive list of fracturing-fluid candidates. Among them, energized fluids are defined as fluids containing at least one compressible, sometimes soluble, gas phase. Energized fluids can be either single-phase, such as CO_2, N_2, and liquefied petroleum gas (LPG); or multiphase, such as foams. For foams, the continuous external phase can be water, oil, or a viscoelastic surfactant formulation. The discontinuous internal phase is typically CO_2 or N_2. Numerous authors have shown the benefits of using energized fluids in the field (King 1985; Mazza 2001; Tudor et al. 2009; Burke et al. 2011). The main advantages of these fluids include (1) limiting the amount of liquid placed in the rock matrix, (2) improving the fluid recovery (caused by the presence of free gas and soluble gas coming out of solution), and (3) minimizing the contact between water-sensitive clays and fines.

Why Current Models Are Not Suited for Energized Fracture Design. Several 3D fracturing models are routinely used for designing incompressible water-based fracturing treatments. However, these models are unable to capture the thermal and compositional effects that are important when using energized fluids. Typically, the fracturing fluid is assumed to be isothermal, with the fluid properties evaluated at the reservoir temperature. A volume balance is performed on the fracturing fluid to track the amount of fluid leakoff and fluid injected, but both the density and the composition of the fluid remain constant. The leakoff rate is assumed to be the same for the entire fluid, which is not compatible with experimental evidence supporting that gas leaks off more slowly than water (Harris 1985, 1987; Ribeiro and Sharma 2012). The only notable exception is the compositional 2D hydraulic fracturing simulator recently developed by Friehauf and Sharma (2009). Their model incorporated, for the first time, the thermal and compositional effects in addition to fracture mechanics and proppant transport in the fracture. The main limitation of their model was the simplified treatment of the geomechanical problem, because the fracture was constrained to a constant height and elliptical shape, referred to as PKN geometry (Nordgren 1972).

Advantages and Limitations of the New Model. The main objective of this paper is to introduce a new compositional model that is particularly suitable for designing and optimizing energized fracture treatments. This new model does not replace conventional fracturing simulators, which offer many additional features. **Table 1** draws a comparison between a typical commercial hydraulic fracturing—the 2D compositional simulator developed by Friehauf and Sharma (2009)—and the new 3D compositional simulator. The table addresses some of the capabilities of the various models and their suitability for various design tasks. Commercial simulators offer a wide range of capabilities, and the list of properties described in Table 1 does not intend to be exhaustive. For instance, several new models are capable of propagating multistage horizontal fractures. The compositional model does not have such capabilities. As of now, it is limited to the propagation of a single fracture in a vertical well. The purpose of this new model is to screen fracturing fluids and to design energized treatments. The additional complexity of the model is particularly suited for describing the performance of energized fluids. For incompressible single-phase fluids, the additional model complexity is not justified.

Model Formulation

Problem Definition. This section introduces the equations that are required to solve the compositional model. **Fig. 1** lists the

Copyright © 2013 Society of Petroleum Engineers

This paper (SPE 159812) was accepted for presentation at the SPE Annual Technical Conference and Exhibition, San Antonio, Texas, USA, 8–10 October 2012, and revised for publication. Original manuscript received for review 18 June 2012. Revised manuscript received for review 30 January 2013. Paper peer approved 4 February 2013.

TABLE 1—COMPARISON OF HYDRAULIC FRACTURING SIMULATORS

Parameter	Commercial Simulators*	Freihauf and Sharma (2009)	New 3D Compositional Model
Fracture shape	Pseudo 3D, 3D planar, or fully 3D	2D elliptical PKN	3D planar
Fracture initiation	Vertical, deviated, and horizontal wells	Vertical wells only	Vertical wells only
Multiple fractures	Multiple clusters available	Single cluster	Single cluster
Fracture propagation	Stress intensity factors	Global mass balance	Stress intensity factors
Temperature	Isothermal	From energy-balance Eq.	From energy-balance Eq.
Fluid density	Constant	Function of (*P, T*)	Function of (*P, T*)
Wellbore hydraulics	Foam option	Multiphase	Multiphase
Proppant setting	Numerous single-phase options	Homogeneous	Phase-dependent
Leakoff	Single phase	Phase-dependent	Phase-dependent

* Commercial simulators also offer numerous enhanced capabilities such as hindered settling, cluster settling, etc.

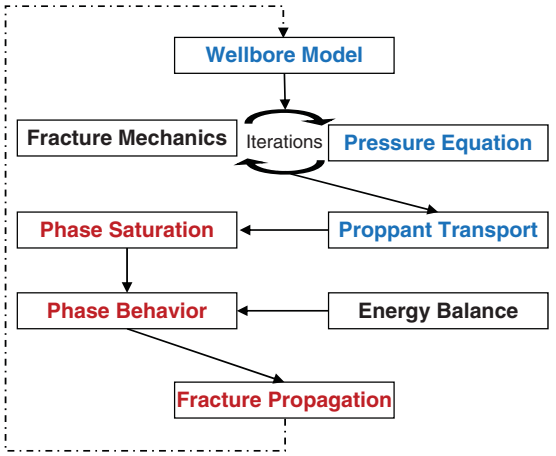

Fig. 1—Simplified version of the main algorithm implemented in the new 3D compositional hydraulic fracturing simulator. Black indicates equations that are used in conventional simulators; blue indicates equations that are modified to account for multiphase, compressible fluids; and red indicates new equations.

constitutive equations of the model. The fracture is assumed to be planar, vertical, and symmetric with respect to the wellbore (biwing). The fracture propagates in a purely elastic medium. There is no assumption regarding the shape of the fracture, which can grow both in length and in height. Fracture width is negligible compared to fracture height and length. The 3D fracture is thus represented by a 2D plane. The fracturing fluid is assumed to flow between essentially parallel porous walls. Fluid flow is idealized as that of a 2D, laminar, compressible, power-law fluid. The fracturing fluid consists of a number of NP fluid phases and a number of NC components distributed among these NP phases. Energized fluids are either single-phase or two-phase mixtures, so NP is equal to 1 or 2.

The right side of **Fig. 2** shows some of the notation introduced for two-phase fluids. As indicated in the Nomenclature, the subscript * refers to a slurry property, which includes proppant. For example, ρ_1^* refers to the density of slurry phase 1 (which contains fluid phase 1 and the proppant carried by fluid phase 1), whereas ρ_1 refers to the density of fluid phase 1 only. S_j^* refers to the saturation of slurry phase j on a total slurry basis (fluid + proppant), and S_j refers to the saturation of fluid phase j on a total fluid basis. γ_j denotes the proppant concentration (volume fraction) in slurry phase j. The component split between the two phases is governed by local thermodynamic equilibrium. K_γ is defined as the ratio of the proppant concentration in the two phases.

Fracture Mechanics. Assuming an isotropic, homogeneous, elastic medium, the 3D elasticity problem is essentially the Navier-Cauchy problem relating strains to applied stresses. Under these assumptions, the problem reduces to the tensile mode-I fracture-opening equation. For planar fractures, the fracture-opening equation is a boundary integral equation that relates the pressure on the crack faces to the crack opening (Kossecka 1971; Bui 1977; Weaver 1977). The equation involves a boundary integral formulation because a local stress applied at a given location deforms the entire surface of the elastic body. We follow the work of Gu (1987), Ouyang (1994), and Yew (1997) to solve the fracture-opening equation using finite-element techniques. The criterion for fracture propagation is based on stress-intensity calculations (Mastrojannis et al. 1979). This formulation differs significantly from 2D models, which require that the fracture boundary in the plane of propagation be specified in advance.

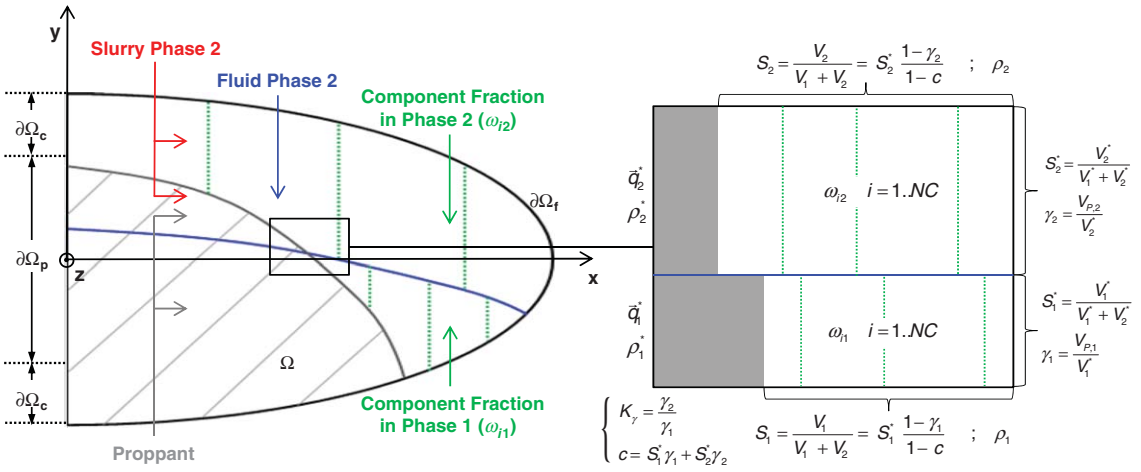

Fig. 2—Definition of the problem and main variables for two-phase fluids carrying proppant.

Fractional-Flow Equations. The fluid-flow equations relate the flow of the fluid in the fracture to the fluid-pressure gradients. Each slurry phase can flow at a different velocity and can have a different rheology. The slurry-phase rheology depends on both the fluid rheology and the proppant concentration in that slurry phase. Because of proppant settling (in the *y*-direction) and proppant retardation (in the *x*-direction), the fluid and the proppant contained in each slurry phase may travel at different velocities. Phase-dependent retardation factors in the *x* and *y*-directions ($\lambda_{j,x}$ and $\lambda_{j,y}$) are introduced so that proppant fluxes can be expressed in terms of slurry fluxes. Conversely, the fluid phase itself has a different velocity than its slurry counterpart.

Each phase is assumed to behave locally as a power-law fluid with known power-law index and consistency. This assumption is not a significant limitation, because different power-law parameters can be specially assigned at each node. Introducing the parameter A_j^* (Eq. 1) that relates the flowrate per unit height of the slurry phase *j* (including proppant) to the gradient of the flow potential, the fractional-flow equations (Eq. 2) are given for the slurry phase *j*, the proppant in phase *j*, and the fluid phase *j*, respectively. Similar equations are derived in the *y*-direction.

$$A_j^* = -\frac{n_j}{2n_j+1} k_j^{\frac{-1}{n_j}} \left(\frac{w^{\frac{2n_j+1}{n_j}}}{2^{\frac{n_j+1}{n_j}}} \right) \left[\left(\frac{\partial P}{\partial x} \right)^2 + \left(\frac{\partial P}{\partial y} + \rho_j^* g \right)^2 \right]^{\frac{1-n_j}{2n_j}} \quad \cdots\cdots\cdots\cdots\cdots\cdots (1)$$

$$\begin{cases} q_{j,x}^* = A_j^* S_j^* \left(\dfrac{\partial P}{\partial x} \right) \\ q_{p,j,x} = q_{j,x}^* \gamma_j \lambda_{j,x} \\ q_{j,x} = q_{j,x}^* \left[(1-\gamma_j) + \dfrac{\rho_p}{\rho_j} \gamma_j (1-\lambda_{j,x}) \right] \end{cases} \quad \cdots\cdots\cdots\cdots (2)$$

Pressure Equation. The overall continuity equation expresses the conservation of mass for compressible, multiphase slurry mixtures. The mass flux is the sum of the contributions of the NP slurry phases. The resulting equation takes the form of a diffusivity equation for pressure (Eq. 3). Because only natural boundary conditions are specified and because the pressure equation only involves pressure gradients, the equation is singular, and the solution is determined within an arbitrary constant. The arbitrary constant is determined from the requirement that the fracture propagates at each timestep (Yew 1997).

$$\begin{aligned} &\frac{\partial}{\partial t}\left\{ w \left(\sum_{j=1}^{NP} \rho_j^* S_j^* \right) \right\} + \frac{\partial}{\partial x}\left\{ \left(\sum_{j=1}^{NP} \rho_j^* A_j^* S_j^* \right) \frac{\partial P}{\partial x} \right\} \\ &+ \frac{\partial}{\partial y}\left\{ \left(\sum_{j=1}^{NP} \rho_j^* A_j^* S_j^* \right) \frac{\partial P}{\partial y} \right\} + \frac{\partial}{\partial y}\left\{ \left(\sum_{j=1}^{NP} \rho_j^{*2} A_j^* S_j^* \right) g \right\} \\ &+ \sum_{j=1}^{NP} \frac{2 C_{w,j} \rho_j}{\sqrt{t-\tau}} = 0; \quad \begin{cases} A^* \dfrac{\partial P}{\partial n} = 0 & \text{on } \partial\Omega_f \text{ and } \partial\Omega_c \\ A^* \dfrac{\partial P}{\partial n} = (\rho^* q_x)_{inj} & \text{on } \partial\Omega_f \end{cases} \end{aligned} \quad \cdots\cdots\cdots\cdots (3)$$

Proppant-Transport Equation. The relative motion of proppant with respect to its slurry counterpart results from gravity, wall, and proppant effects, as shown by Liu (2006). The retardation factors in the *x* and *y*-directions ($\lambda_{j,x}$ and $\lambda_{j,y}$) are phase-dependent, and their expressions are provided by Friehauf (2009). The values of $\lambda_{j,x}$ and $\lambda_{j,y}$ for single-phase fluids were obtained from experimental data (Liu 2006). In this model, the proppant split between two phases (γ_2/γ_1) is defined by the user, and K_γ can be seen as a modeling parameter to determine how the proppant is distributed within the two phases. Therefore, Eq. 4, expresses that the unsteady proppant-transport equation can be solved in terms of the overall proppant concentration *c*. The literature on the physics of proppant transport by complex multiphase fluids is scarce. We follow here the work of Valkó and Economides (1997). Additional laboratory work is nonetheless required to properly characterize retardation factors and proppant split for two-phase fluids.

$$\begin{aligned} &\frac{\partial}{\partial t}(wc) + \frac{\partial}{\partial x}\left\{ \sum_{j=1}^{NP} \gamma_j \lambda_{j,x} A_j^* S_j^* \left(\frac{\partial P}{\partial x} \right) \right\} \\ &+ \frac{\partial}{\partial y}\left\{ \sum_{j=1}^{NP} \gamma_j \lambda_{j,x} A_j^* S_j^* \left(\frac{\partial P}{\partial y} + \rho_j^* g \right) \right\} \\ &= 0 \; ; \begin{cases} \dfrac{\partial c}{\partial n} = 0 & \text{on } \partial\Omega_f \text{ and } \partial\Omega_c \\ c = c_{\text{inj}} & \text{on } \partial\Omega_f \end{cases} \quad \text{and } c \le 0.52. \end{aligned} \quad \cdots\cdots\cdots\cdots (4)$$

Energy-Balance Equation. An energy-balance equation is used to model the heat transfer occurring between the fracturing fluid and the reservoir. A rigorous treatment of heat transfers becomes important as changes in temperature affect the fracturing-fluid composition, density, and rheology. The total energy flux is the sum of the contributions of the NP slurry phases. Assuming that these contributions are linearly independent, the following unsteady conservation energy equation is derived (Eq. 5):

$$\begin{aligned} &\frac{\partial}{\partial t}\left\{ Tw \left(\sum_{j=1}^{NP} S_j^* \rho_j^* C_{p,j}^* \right) \right\} + \frac{\partial}{\partial x}\left\{ T \left(\sum_{j=1}^{NP} q_{j,x}^* \rho_j^* C_{p,j}^* \right) \right\} \\ &+ \frac{\partial}{\partial y}\left\{ T \left(\sum_{j=1}^{NP} q_{j,y}^* \rho_j^* C_{p,j}^* \right) \right\} + \frac{2}{\sqrt{t-\tau}}\left\{ T \left(\sum_{j=1}^{NP} \rho_j C_{p,j} C_{w,j} \right) \right\} \\ &+ \frac{2}{\sqrt{t-\tau}} \sqrt{\frac{K_R \rho_R C_{p,R}}{\pi}} (T - T_R) = 0; \\ &\begin{cases} \dfrac{\partial T}{\partial n} = 0 & \text{on } \partial\Omega_f \text{ and } \partial\Omega_c \\ T = T_{\text{inj}} & \text{on } \partial\Omega_f \end{cases} \\ &\text{where } C_{p,j}^* = \frac{(1-\gamma_j)\rho_j C_{p,j} + \gamma_j \rho_p C_{p,\text{prop}}}{\rho_j^*}. \end{aligned} \quad \cdots\cdots\cdots (5)$$

Component Mass-Conservation Equations. For multiphase mixtures, each component can be transported by fluid phases flowing at different velocities. The fluid phase itself has a different velocity than its slurry counterpart because of proppant settling and retardation. The conservation of mass is applied to each component *i*. ω_{ij} is the mass fraction of component *i* in phase *j*. There are NC components, so there are NC mass conservation equations given in Eq. 6:

$$\begin{aligned} &\frac{\partial}{\partial t}\left[w \left(\sum_{j=1}^{NP} \omega_{ij} \rho_j (1-\gamma_j) S_j^* \right) \right] + \frac{\partial}{\partial x}\left[\sum_{j=1}^{NP} \omega_{ij} \rho_j q_{j,x} \right] \\ &+ \frac{\partial}{\partial y}\left[\sum_{j=1}^{NP} \omega_{ij} \rho_j q_{j,x} \right] + \frac{2}{\sqrt{t-\tau}} \sum_{j=1}^{NP} C_{w,j} \omega_{ij} \rho_j = 0; \\ &\begin{cases} q_j = 0 & \text{on } \partial\Omega_f \text{ and } \partial\Omega_c \\ \omega_{ij} = \omega_{ij,\text{inj}} & \text{on } \partial\Omega_f \end{cases} \end{aligned} \quad \cdots\cdots\cdots\cdots (6)$$

For single-phase fluids, the NC mass-conservation equations are not required because the fluid composition remains constant. For two-phase mixtures, Eq. 6 may be solved for the mass fraction z_i ($i = 1 \ldots \text{NC}$) or in terms of fluid saturations. For traditional foams, there are only two components and two phases, and the water component does not partition in the gas-like phase. In that case, Eq. 6 appears to be more stable when solved for fluid saturation. For N_2 foams, the liquid phase only contains water, and the gas phase only contains nitrogen. For CO_2 foams, the liquid phase contains water and some soluble CO_2, and the gas phase only contains CO_2. The amount of soluble CO_2 is predicted by the *k*-value K_2, which is the mass fraction of CO_2 in the gas phase divided by

the mass fraction of CO_2 in the liquid phase. The value of K_2 is derived from a fit of solubility data under a given range of pressures and temperatures. For N_2 foams, $1/K_2$ is simply equal to 0. For foams, Eq. 6 is rewritten as Eq. 7, which is solved numerically for the saturation of the liquid phase (S_1).

$$\frac{\partial}{\partial t}\{S_1 w(1-c)(1-1/\overline{K}_2)\rho_1\} + \frac{\partial}{\partial x}\left\{S_1(1-c)\rho_1 A_1^* \alpha_{1,x}(1-1/\overline{K}_2)\left(\frac{\partial P}{\partial x}\right)\right\} + \frac{\partial}{\partial y}\left\{S_1(1-c)\rho_1 A_1^* \alpha_{1,y}(1-1/\overline{K}_2)\left(\frac{\partial P}{\partial y}+\rho_1^* g\right)\right\} + \frac{2}{\sqrt{t-\tau}}\{\rho_1 C_{w,1}(1-1/\overline{K}_2)\} = 0; \quad \text{where } \alpha_{j,x} = 1+\frac{\rho_p}{\rho_j}\frac{\gamma_j}{1-\gamma_j}(1-\lambda_{j,x}). \quad \cdots\cdots\cdots\cdots (7)$$

Comments on Foam Stability. For stable foams, the two phases travel at the same velocity and there is no slippage. Consequently, the same power-law parameters are assigned to both phases. From a transport standpoint, stable foam is seen as a single "pseudo-phase." The reader may refer to the work of Reidenbach et al. (1986), Valkó and Economides (1997), and Khade and Shah (2004) for more details on foam rheology. The addition of proppant further complicates the slurry rheology, and the reader may refer to Ribeiro (2013) for empirical correlations describing the rheology of proppant-laden foams. Interfacial forces prevent gravity segregation. This effect is simply modeled by replacing the liquid slurry density (ρ_1^*) by the foam density (ρ_T^*) in the convective term in the y-direction of Eq. 7.

For unstable foams, the interfacial forces are not capable of holding the gas bubbles inside the external liquid phase. As the gas bubbles coalescence, the gas pocket migrates upward because of gravity segregation. After a few minutes, the water and the gas phases are completely separated and the mixture loses its viscosity. Gravity segregation occurs because of the contrast between the liquid and the gas-slurry densities.

Wellbore Model. Operators regularly collect surface temperature and pressure data, but they rarely collect in-situ data. The fracturing-fluid composition and density depend on both temperature and pressure, so variations in temperature and pressure along the wellbore cannot be ignored. Fluid flow and heat transfers in the wellbore have been extensively studied by Hasan and Kabir (2002). The wellbore model used in this model is similar to the one developed by Friehauf (2009). The Peng-Robinson equation of state is implemented to predict the phase behavior of the fluid. Another option that is available is to use the Rachford-Rice procedure for known equilibrium values.

Main Algorithm

Fracture Propagation. Fracture propagation is approximated by an incremental process. For a short period of time, the fracture remains stationary. The fracture front is temporarily arrested by the fracture toughness or by the in-situ stress contrast. During this period, fluid is pumped into the fracture, causing an increase of fluid pressure, fracture width, and stress-intensity factor at the fracture front. When the stress-intensity factor exceeds the fracture toughness, the fracture front propagates. We follow the work of Yew (1997) for propagating the fracture dynamically using specific elements along the fracture tip. The development of the unstructured mesh does not fall in the scope of this paper and the reader should refer to the work of Gu (1987), Ouyang (1994), and Yew (1997) for more details.

The fracture problem is fully solved if we compute the fracture geometry, fluid composition, fluid temperature, fluid pressure, and proppant distribution. The set of equations presented here constitutes a complete set of independent equations, for which the number of independent equations equals the number of independent variables. Therefore, the compositional fracture problem is mathematically well-posed, and a numerical solution is possible and has been implemented in the new 3D compositional simulator. Fig 2 shows a simplified version of the main algorithm. Eqs. 3 through 6 (or 7) are solved with a finite-element method. A variational statement of the equations is obtained by solving the strong form of the equations in the sense of weighted averages. A Galerkin finite-element method is employed to numerically solve these equations.

Time Scheme. The time derivatives are approximated by an implicit backward finite-differencing scheme. The main reason behind this choice is that the timestep Δt^n is not chosen arbitrarily, but is calculated from the compatibility condition (Eq. 8). An implicit scheme is thus preferred because this scheme is unconditionally stable. For each timestep, the increase in fracture mass must be equal to the mass of fluid pumped minus the mass of fluid that leaked off. A similar compatibility condition was derived for incompressible fluids by Gu (1987) and Yew (1997) on a volume basis. Because the fracturing fluid is now compressible, the new timestep requirement is derived from the overall mass conservation:

$$\Delta t^n = \frac{\Delta m_{\text{fracture}} + \Delta m_{\text{leakoff}}}{\dot{m}_{\text{pumped}}}. \quad \cdots\cdots\cdots\cdots\cdots (8)$$

The timestep derived from the compatibility equation and used in the diffusivity equation (Eq. 3) may be too large for convection-dominated equations (Eqs. 4 through 7), which are numerically more unstable. As the fracture grows, the calculated timestep increases exponentially. A new time-decoupling scheme is introduced. First, the fracture mechanics, the pressure equation, and the compatibility equation are solved together using an iterative scheme, which follows the Picard iteration method (successive substitutions). Then, a forward time loop is used to solve numerically the three convection-dominated equations. The user can prescribe a small timestep to improve numerical stability.

For all the simulations presented in this paper, the simulator was run on a standard desktop PC. The computing time was less than 2 minutes, which makes the model attractive for design purposes. A graphic user interface is used to input the pumping schedule and the reservoir properties, and to output the fracture geometry.

Model Validation. To verify the new model, multiple comparisons have been made with existing analytical solutions and with a well-established commercial 3D fracturing simulator for single-phase, incompressible fluids. Three examples, referred to as Cases A, B, and C, are intended to provide a direct comparison with predictions of the 2D analytical models. Case A corresponds to radial fracture propagation, whereas Cases B and C correspond to PKN-like fracture propagation without and with fluid leakoff (0.002 ft/$\sqrt{\text{min}}$), respectively. For the three cases, the fluid was assumed to be single-component, single-phase, incompressible, isothermal, and Newtonian. **Fig. 3** shows the vertical stress distributions for the different cases. Three layers are modeled with the perforated target zone located between the bounding layers. **Table 2** shows the different inputs used in the simulations.

Radial Fracture Propagation (Case A). The stress distribution is constant (5,000 psi) across the three layers in Case A (Fig. 3). The stress barriers at the interfaces are removed so that the perforation interval can be seen as a point source. When the vertical distribution of the in-situ horizontal minimum stress is uniform, the fracture is expected to take the shape of a circle in the x-y plane. **Fig. 4** shows the width profile at the end of pumping predicted by the new model. As expected, the fracture follows a circular shape, and the fracture length is equal to the fracture height. As shown in **Fig. 5,** the growth of the circular fracture compares very well with (1) the analytical expression derived by Geertsma and de Klerk (1969) for radial fractures with no leakoff, and (2) with the numerical solution obtained with the commercial 3D simulator.

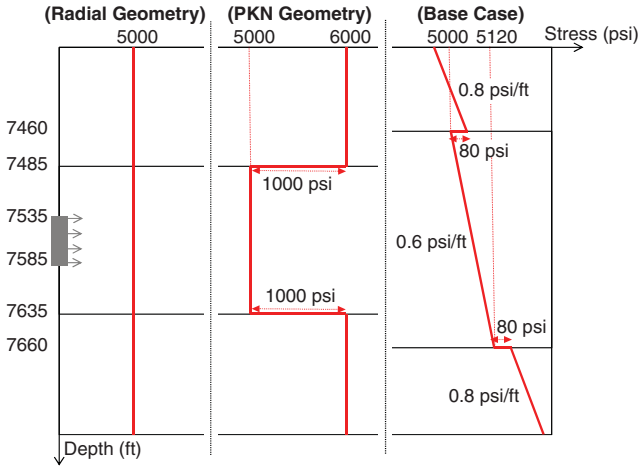

Fig. 3—In-situ horizontal stress distribution along the well for radial, PKN, and base cases.

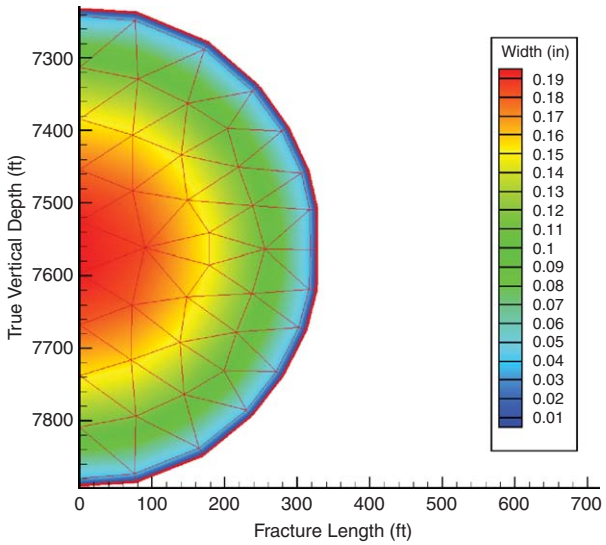

Fig. 4—Final width profile (radial case, no fluid leakoff).

PKN-Like Fracture Propagation (Cases B and C). When a large stress contrast occurs at the interface with the bounding layers, the fracture height is bounded by the pay-zone height. The PKN elliptical-shape model analytical derived by Nordgren (1972) has been regarded as best suited for long, constant-height fractures. In Cases B and C, strong stress barriers are introduced (1,000 psi) to maintain a constant fracture height. The fluid leakoff was set to zero for Case B and was set to 0.002 ft/$\sqrt{}$min for Case C. **Figs. 6 and 8** show the width profile at the end of pumping predicted by the new model for the non-leakoff and the leakoff cases. As expected, the fractures are well-constrained in

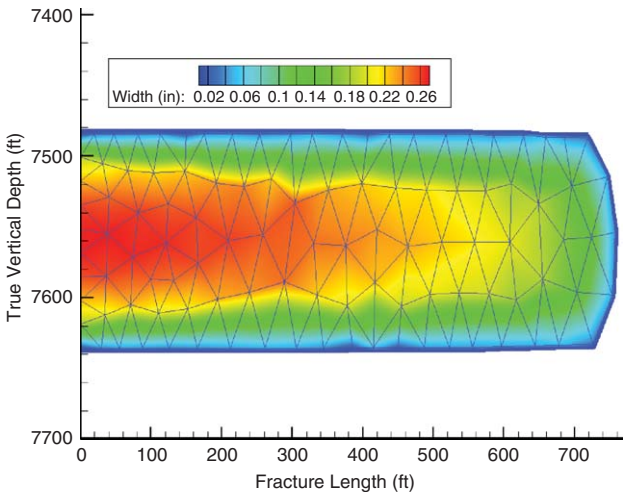

Fig. 6—Final width profile (PKN case, no fluid leakoff).

TABLE 2—INPUT PARAMETERS FOR MODEL VALIDATION (CASES A, B, AND C)

Parameter	Case A	Case B	Case C
Pumping time (min)	30	30	30
Injection flow rate (bbl/min)	20	20	20
Viscosity (cp)	40	40	40
Pay zone height (ft)	∞	150	150
Stress contrast (psi)	/	1000	1000
Young's modulus, psi ($\times 10^6$)	2.5	2.5	2.5
Poisson's ratio	0.25	0.25	0.25
Leakoff coefficient (ft/$\sqrt{}$min)	0	0	0.002*

* Please note that the only difference between Cases B and C is the value of the leakoff coefficient.

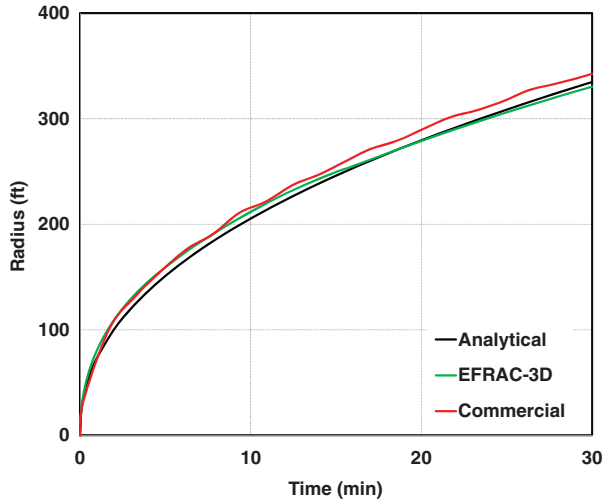

Fig. 5—Fracture propagation over time (radial case, no fluid leakoff).

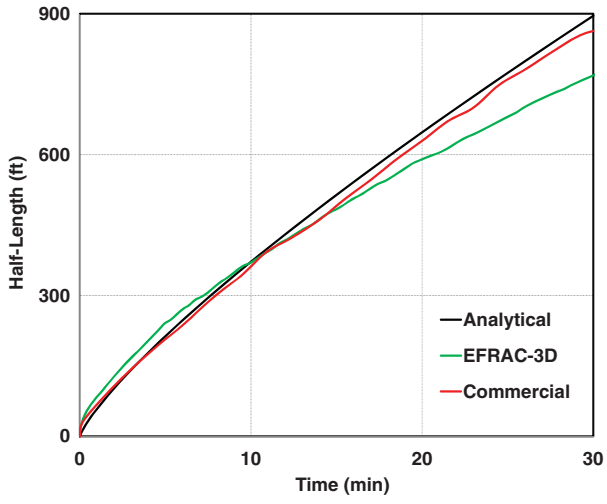

Fig. 7—Fracture propagation over time (PKN case, no fluid leakoff).

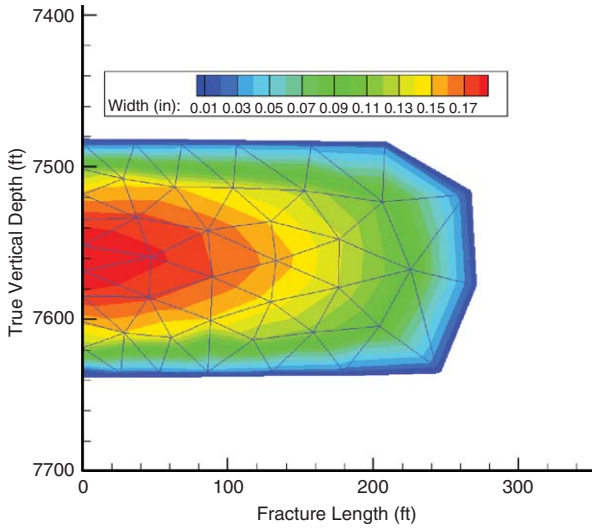

Fig. 8—Final width profile (PKN case, fluid leakoff).

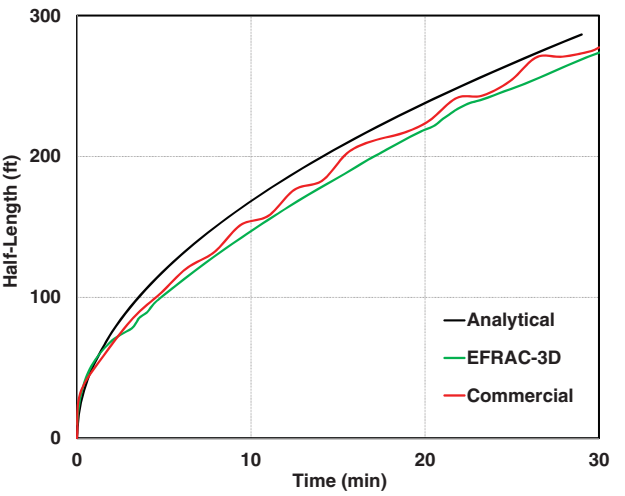

Fig. 9—Fracture propagation over time (PKN case, fluid leakoff).

height, and the fracture width tends to follow an elliptical shape. Because this is well-established, fluid leakoff is one of the most critical parameters in fracture design. As the leakoff increases from 0 to 0.002 ft/$\sqrt{}$min, the fracture half-length decreases from 770 to 275 ft, and the maximum fracture width decreases from 0.27 to 0.19 in.

Figs. 7 and 9 show fracture growth predicted by (1) the analytical solution derived by Nordgren (1972), (2) the commercial 3D simulator, and (3) the new model. For Case C, the new model compares well with the pre-existing predictions (Fig. 9). The final width profile (Fig. 8) clearly follows an elliptical shape, and the mesh is not distorted. For Case B (no fluid leakoff), the match is not as good but remains satisfactory (Fig. 7). As seen in Fig. 6, the final mesh contains several elongated elements and the width profile is not as elliptical. A better fit could have been obtained using a finer mesh, but mesh refinement is out of the scope of this paper. Both the numerical solutions obtained by the commercial simulator and the new 3D compositional model are lower than the analytical solution. This is not surprising, because the analytical solution is known to overestimate crack opening near the crack front.

The few comparisons presented in this paper show that the new model can be validated against well-established models under some restrictive assumptions. The radial and the PKN geometries constitute the two ends of the spectrum for single-layer facture propagation. The PKN model is more applicable for long-duration treatments, whereas the radial model is applicable at early times, when the stress boundaries are not affecting fracture propagation.

Energized Example Cases

Our primary goal is to apply the new model to cases for which prior models do not apply (i.e., energized fractures). Three example cases (D, E, and F) are run to see how the model may be used as a design tool. Cases D, E, and F correspond to the injection of gelled water, gelled LPG, and gelled CO_2, respectively. For the three examples, the stress distribution is the same and is referred to as "Base Case" in Fig. 3. The stress distribution is more realistic than the simplistic radial and PKN stress distributions used for model validation. The fracture gradient is equal to 0.6 psi/ft in the pay zone and to 0.8 psi/ft in the bounding layers. A stress contrast of 80 psi is present at the interfaces. This representation is typical of many reservoirs, for which the basement and overburden layers are frequently stiffer than the target rock. For simplicity, the leakoff coefficient is assumed to be the same for the three cases. The value is typical of gelled fluids in tight-gas reservoirs (0.0005 ft/$\sqrt{}$min in the pay zone and 10^{-7} ft/$\sqrt{}$min in the bounding layers). Also, the changes occurring in the wellbore are not included in this paper. The injection flow rate and the injection temperature are the same for the water, LPG, and CO_2 cases.

Design of Energized Treatments (Cases D, E, and F). The gelled-water case is included for comparison purposes. The reservoir properties and the pumping schedule are the same for the water, LPG, and CO_2 cases, as shown in **Table 3.** The specific fluid properties are given on the right side of Table 3. These properties are given at a temperature of 50°F and a pressure of 5,000 psi simply for reference; they are actually evaluated as a function of pressure and temperature in the model. For the three cases, the fluid pressure in the fracture was above the critical pressure. There was no change of state. **Figs. 10, 12, and 13** show the width profile at the end of pumping (at 30 min) for the water, LPG, and CO_2 cases, respectively. **Fig. 11** shows the final temperature for the water case. As expected, the fluid temperature equals the reservoir temperature along the fracture tip, and the fluid temperature is cooler near the perforations. **Fig. 14** shows the total fracture

TABLE 3—INPUT PARAMETERS FOR ENERGIZED EXAMPLE CASES (CASES D THROUGH H)

Parameter	Cases D–H	Parameter	Case D	Case E	Cases F, G, H
Pumping time (min)	30	Fluid type	Water	LPG	CO_2
Injection flow rate (bbl/min)	30	Density* (lbm/ft^3)	63.3	35.2	64.9
Pay zone height (ft)	200	Viscosity at 51 ft s^{-1}* (cp)	40	14	17
Stress contrast (psi)	80	Heat capacity* (BTU/lbm-°F)	1	0.45	0.35
Young's modulus, psi ($\times 10^6$)	2.5	Leakoff coefficient (ft/$\sqrt{}$min)	0.0005	0.0005	0.0005
Poisson's ratio	0.25	Injection temperature (°F)	50	50	50
Reservoir temperature (°F)	200				

* Fluid properties evaluated at $P = 5{,}000$ psi and $T = 50$°F

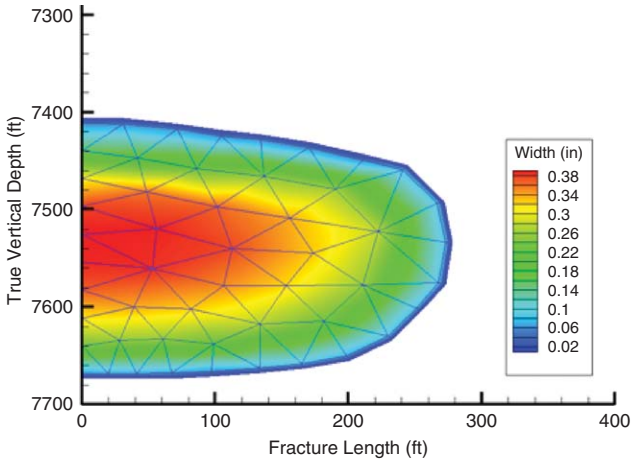

Fig. 10—Final width profile (base stress, water).

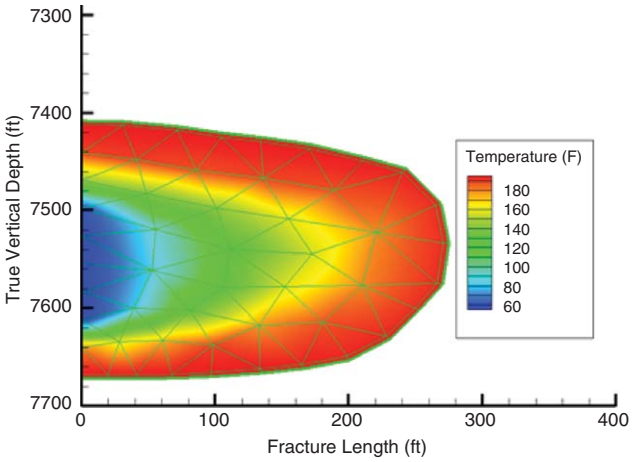

Fig. 11—Final temperature profile (base stress, water).

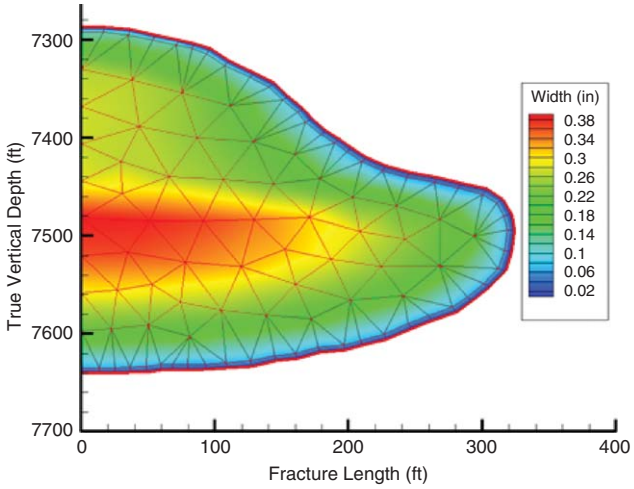

Fig. 12—Final width profile (base stress, LPG).

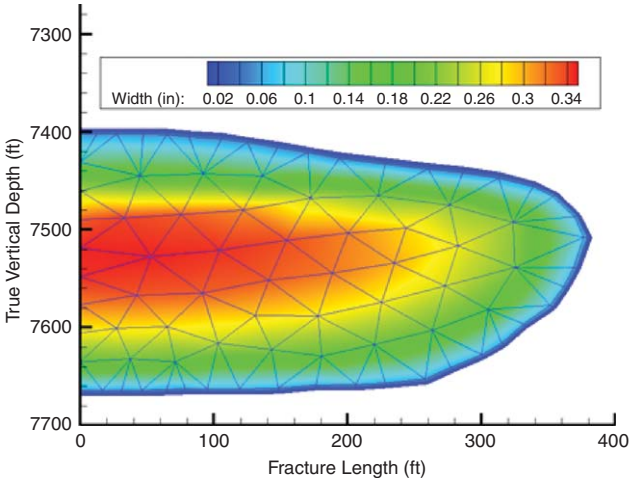

Fig. 13—Final width profile (base stress, CO_2).

length (twice the fracture half-length) and the maximum fracture width vs. time for the water, LPG, and CO_2 cases. The solid lines represent fracture lengths, and the dotted lines represent maximum fracture widths.

For the three cases, the fracture does not penetrate the lower layer, which offers a larger resistance (higher stress). Rather, the fracture grows upward as the stress decreases in the pay zone. The stress contrast is relatively small at the interface so the fracture can overcome the stress contrast and penetrate the upper lower. Vertical migration is particularly important for the LPG case. Under these specific conditions, the density contrast between the fracturing fluid and the in-situ stress promotes upward growth. Upward growth nonetheless affects fracture opening in the three cases, and the fractures are thinner than predicted by the PKN model.

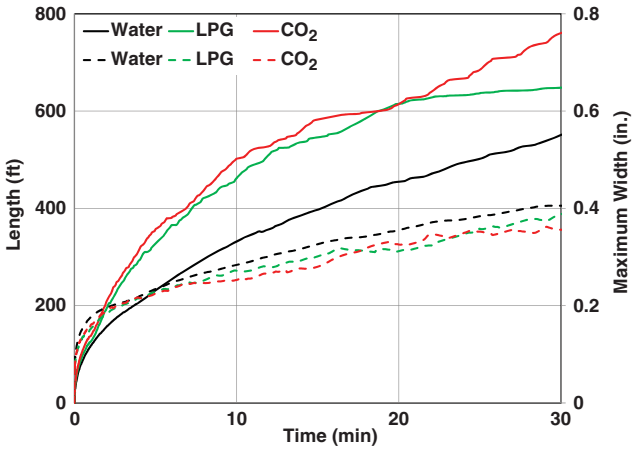

Fig. 14—Fracture length (solid lines) and maximum width (dotted lines) over time for water, LPG, and CO_2. The plot shows how the fracturing fluid impacts fracture geometry.

Even though the same volume of water, LPG, and CO_2 is injected, the final fracture volumes are different because of density variations. As the temperature rises in the fracture from 50 to 200°F, and the pressure changes by approximately 200 psi, the density decreases from 63.4 to 62.5 lbm/ft^3 for water, from 35.5 to 30.3 lbm/ft^3 for LPG, and from 65.9 to 44.5 lbm/ft^3 for CO_2. Significant fluid expansion leads to larger fracture volumes for the LPG and CO_2 cases as compared with the water case. This effect is not captured by traditional isothermal fracturing simulators.

Furthermore, fluid viscosity changes as temperature and pressure change. As seen in Table 3, gelled LPG and gelled CO_2 are significantly less viscous than gelled water. The viscosity difference increases even more as the fracturing fluid heats up. The viscosity difference contributes to make the fractures longer and thinner for LPG and CO_2 as compared with water. This is why the maximum width of the CO_2 and the LPG fractures is lower than the water fracture even though the CO_2 and LPG fractures have a larger volume than the water fracture. The fracture is better constrained and wider in the water case. These results are in agreement with the common observation that viscous fluids tend to create shorter and wider fractures with minimum vertical migration.

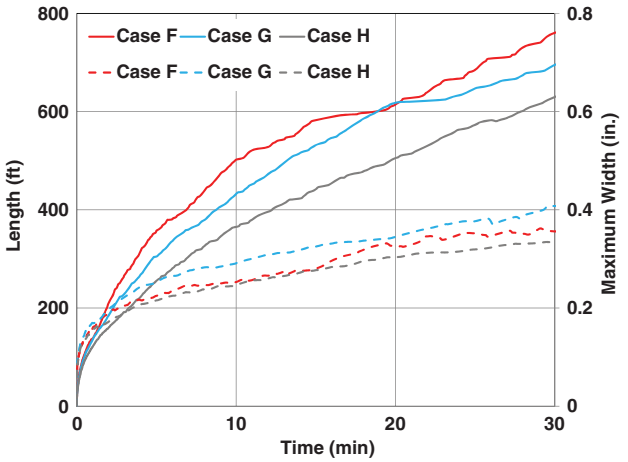

Fig. 15—Fracture length (solid lines) and maximum width (dotted lines) over time for cases F, G, and H. The plot shows the impact of fluid expansion and viscosity reduction.

Comparison of Non-Isothermal and Isothermal Models (Cases F, G, and H). The following comparison intends to show more specifically how changes in viscosity and density alone alter fracture growth. As seen in Tables 2 and 3, Cases F, G, and H correspond to the same pumping schedule and the same reservoir conditions. The only difference is that the simulations are made under different assumptions. Case F is the case presented previously, accounting for density and viscosity variations. Case G accounts for density changes, but the fluid viscosity is assumed to be constant. In Case H, fluid density and viscosity are assumed to remain constant. This is the assumption typically made by commercial fracturing simulators. **Fig. 15** shows the total fracture length (twice the fracture half-length) and the maximum fracture width vs. time for these three cases. When fluid expansion is accounted for, fracture growth is significantly increased (698 vs. 633 ft). If both fluid expansion and viscosity reduction are accounted for, the fracture becomes even longer (763 vs. 698 ft) and thinner (0.35 vs. 0.41 in.) because the viscosity decreases as the fluid heats up. This comparison shows that it is critical to account for density and viscosity changes when designing fracturing treatments with compressible fluids such as CO_2 or LPG. This example illustrates some of the limitations of traditional isothermal simulators and how they compare with this new non-isothermal simulator.

Conclusion

This paper introduced a new 3D compositional model for hydraulic fracturing. The model captured the thermal and compositional changes occurring in the fracturing fluid. The model is valid for any number of components and for both single-phase compressible fluids (such as N_2, CO_2, and LPG) and two-phase fluids (foams). A 2D proppant equation was implemented to predict proppant placement inside the fracture.

The model was validated for traditional fracture geometries (radial and PKN) and for traditional fluid formulations (incompressible water-based fluids). Examples illustrated the capabilities and the usefulness of the model with cases for which prior 3D models do not apply (i.e., energized fractures). In particular, the model showed how fluid expansion and viscosity reduction impacted fracture growth.

This new model does not intend to replace conventional fracturing simulators, which offer many additional features. Rather, it constitutes another tool available to the fracturing engineer to screen fracturing fluids and to design energized treatments. In many unconventional reservoirs, energized fluids are thought to outperform water treatments but, until now, no commercial tool was available to design or analyze such treatments. The new energized model can be combined with a productivity model (Friehauf et al. 2010) to quantify the potential benefits introduced by energizing the fracturing fluid. This tool enables us to design engineered fracturing treatments.

Nomenclature

A_j^* = intermediate variable for slurry phase j defined by Eq. 1, ft^5/(lbf-min)
c = proppant concentration (volume fraction)
$C_{p,j}$ = heat capacity of fluid phase j, BTU/(lbm-°F)
$C_{p,j}^*$ = heat capacity of slurry phase j, BTU/(lbm-°F)
$C_{p,\mathrm{prop}}$ = heat capacity of proppant, BTU/(lbm-°F)
$C_{p,R}$ = heat capacity of reservoir rock, BTU/(lbm-°F)
$C_{w,j}$ = leakoff coefficient of fluid phase j, ft/$\sqrt{\text{min}}$
g = gravity of earth, ft/s^2
k_j = flow consistency index of slurry phase j, lbm-min^n/ft^2
$k_{\mathrm{ret},j}$ = retardation factor for slurry phase j in the horizontal direction
K_i = K-value for component i (component split between phases 1 and 2)
K_R = thermal conductivity of rock, BTU/(min-ft-°F)
K_γ = proppant split between two phases (γ_2/γ_1)
$q_{j,x}$, $q_{j,y}$ = flowrate per unit height of fluid phase j in the horizontal and vertical direction, ft^2/min
$q_{j,x}^*$, $q_{j,y}^*$ = flowrate per unit height of slurry phase j in the horizontal and vertical direction, ft^2/min
$q_{L,j}^*$ = fluid loss flowrate per unit height of fluid phase j, ft/min
$q_{p,j,x}^*$, $q_{p,j,y}^*$ = flowrate per unit height of proppant in phase j in the horizontal and vertical direction, ft^2/min
m_{pumped} = mass rate imposed at the perforations, lbm/min
n = normal direction
n_j = flow-behavior index of slurry phase j
NC = number of components
NP = number of phases
P = fluid pressure, psi
S_j = saturation of fluid phase j
S_j^* = saturation of slurry phase j
t = time, min
T = fluid temperature, °F
T_R = reservoir temperature, °F
V_P = volume of proppant in the slurry, ft^3
$V_{P,j}$ = volume of proppant in slurry phase j, ft^3
$V_{\mathrm{set},j}$ = settling velocity in slurry phase j, ft/min
V_T = total slurry volume, ft^3
w = fracture width, ft
x = horizontal location, ft
y = vertical location, ft
$\partial\Omega_c$ = non-perforated portion along the wellbore
$\partial\Omega_f$ = fracture front
$\partial\Omega_p$ = perforated interval along the wellbore
γ_j = proppant concentration (volume fraction) in slurry phase j
$\Delta m_{\mathrm{fracture}}$ = change in fracturing fluid mass during Δt^n, lbm
$\Delta m_{\mathrm{leakoff}}$ = mass of fluid that leaked off during Δt^n, lbm
Δt^n = timestep increment, min
$\lambda_{j,x}$, $\lambda_{j,y}$ = retardation factor for proppant in phase j in the horizontal and vertical direction
ρ_j = density of fluid phase j, lbm/ft^3
ρ_j^* = density of slurry phase j, lbm/ft^3
ρ_p = density of proppant, lbm/ft^3
ρ_R = density of reservoir rock, lbm/ft^3
ρ_T^* = density of slurry, lbm/ft^3
τ = retardation factor, min
ω_{ij} = mass fraction of component i in phase j
Ω = fracture surface

Subscripts

i = component i
inj = Dirichlet BCs at the perforations

j = phase j
R = reservoir property

Superscripts

n = timestep n
$*$ = slurry property

Acknowledgments

The authors would like to acknowledge the support provided by the US Department of Energy and the companies sponsoring the JIP on *Hydraulic Fracturing and Sand Control* (Air Liquide, Air Products, Anadarko, Apache, Baker Hughes, BHP Billiton, BP, Chevron, ConocoPhillips, Ferus, Fairmont Minerals, Halliburton, Hess Corporation, Lanxness, Linde, MeadWestvaco, Pemex, Pioneer Natural Resources, Praxair, Saudi Aramco, Schlumberger, Shell, Southwestern Energy, Statoil, Talisman Energy, Total, Weatherford, and YPF) at the University of Texas at Austin.

References

Bui, H.D. 1977. An integral equations method for solving the problem of a plane crack of arbitrary shape. *J. Mech. Phys. Solids* **25** (1): 29–39. http://dx.doi.org/10.1016/0022-5096(77)90018-7.

Burke, L.H., Nevison, G.W., and Peters, W.E. 2011. Improved Unconventional Gas Recovery With Energized Fracturing Fluids: Montney Example. Presented at the SPE Eastern Regional Meeting, Columbus, Ohio, USA, 17–19 August. SPE-149344-MS. http://dx.doi.org/10.2118/149344-MS.

Friehauf, K.E. 2009. *Simulation and Design of Energized Hydraulic Fractures*. PhD dissertation, University of Texas at Austin, Austin, Texas (August 2009).

Friehauf, K.E. and Sharma, M.M. 2009. A New Compositional Model for Hydraulic Fracturing With Energized Fluids. *SPE Prod & Oper* **24** (4): 562–572. SPE-115750-PA. http://dx.doi.org/10.2118/115750-PA.

Friehauf, K.E., Suri, A., and Sharma, M.M. 2010. A Simple and Accurate Model for Well Productivity for Hydraulically Fractured Wells. *SPE Prod & Oper* **25** (4): 453–460. SPE-119264-PA. http://dx.doi.org/10.2118/119264-PA.

Geertsma, J. and de Klerk, F. 1969. A Rapid Method of Predicting Width and Extent of Hydraulic Induced Fractures. *J Pet Technol* **21** (12): 1571–1581. SPE-2458-PA. http://dx.doi.org/10.2118/2458-PA.

Gu, H. 1987. *A Study of Propagation of Hydraulically Induced Fractures*. PhD dissertation, University of Texas at Austin, Austin, Texas (December 1987).

Gupta, S. 2011. Unconventional Fracturing Fluids: What, Where and Why. Presented at the EPA Technical Workshops for the Hydraulic Fracturing Study, Arlington, Virginia, February 2011.

Harris, P.C. 1985. Dynamic Fluid Loss Characteristics of Foam Fracturing Fluids. *J Pet Technol* **37** (10): 1847–1852. SPE-11065-PA. http://dx.doi.org/10.2118/11065-PA.

Harris, P.C. 1987. Dynamic Fluid-Loss Characteristics of CO2-Foam Fracturing Fluids. *SPE Prod Eng* **2** (2): 89–94. SPE-13180-PA. http://dx.doi.org/10.2118/13180-PA.

Hasan, A.R. and Kabir, C.S. 2002. *Fluid Flow and Heat Transfer in Wellbores*. Richardson, Texas: Textbook Series, SPE.

Khade, S.D. and Shah, S.N. 2004. New Rheological Correlations for Guar Foam Fluids. *SPE Prod & Fac* **19** (2): 77–85. SPE-88032-PA. http://dx.doi.org/10.2118/88032-PA.

King, G.E. 1985. Foam and Nitrified Fluid Treatments-Stimulation Techniques and More. Paper SPE 14477 based on a speech presented as a Distinguished Lecture during the 1985–1986 season.

Kossecka, E. 1971. Defects as Surface Distribution of Double Forces. *Archives of Mechanics* **23** (1971): 481–494.

Liu, Y. 2006. *Settling and Hydrodynamic Retardation of Proppants in Hydraulic Fractures*. PhD dissertation, University of Texas at Austin, Austin, Texas (August 2006).

Mastrojannis, E.N., Keer, L.M., and Mura, T. 1979. Stress intensity factor for a plane crack under normal pressure. *Int. J. Fract.* **15** (3): 247–258. http://dx.doi.org/10.1007/bf00033223.

Mazza, R.L. 2001. Liquid-Free CO2/Sand Stimulations: An Overlooked Technology—Production Update. Presented at the SPE Eastern Regional Meeting, Canton, Ohio, USA, 17–19 October. SPE-72383-MS. http://dx.doi.org/10.2118/72383-MS.

Nordgren, R.P. 1972. Propagation of a Vertical Hydraulic Fracture. *SPE J.* **12** (4): 306–314. SPE-3009-PA. http://dx.doi.org/10.2118/3009-PA.

Ouyang, S. 1994. *Propagation of Hydraulically Induced Fractures with Proppant Transport*. PhD dissertation, University of Texas at Austin, Austin, Texas (May 1994).

Reidenbach, V.G., Harris, P.C., Lee, Y.N. et al. 1986. Rheological study of foam fracturing fluids using nitrogen and carbon dioxide. *SPE Prod Eng* **1** (1): 31–41. SPE-12026-PA. http://dx.doi.org/10.2118/12026-PA.

Ribeiro, L.H. and Sharma, M.M. 2012. Multiphase Fluid-Loss Properties and Return Permeability of Energized Fracturing Fluids. *SPE Prod & Oper* **27** (3): 265–277. SPE-139622-PA. http://dx.doi.org/10.2118/139622-PA.

Ribeiro, L.H. 2013. *Design of Energized Hydraulic Fractures*. PhD dissertation, University of Texas at Austin, Austin, Texas.

Tudor, E.H., Nevison, G.W., Allen, S. et al. 2009. 100% Gelled LPG Fracturing Process: An Alternative to Conventional Water-Based Fracturing Techniques. Presented at the SPE Eastern Regional Meeting, Charleston, West Virginia, USA, 23–25 September. SPE-124495-MS. http://dx.doi.org/10.2118/124495-MS.

Valkó, P. and Economides, M.J. 1997. Foam Proppant Transport. *SPE Prod & Fac* **12** (4): 244–249. SPE-27897-PA. http://dx.doi.org/10.2118/27897-PA.

Weaver, J. 1977. Three-dimensional crack analysis. *Int. J. Solids Struct.* **13** (4): 321–330. http://dx.doi.org/10.1016/0020-7683(77)90016-6.

Yew, C.H. 1997. *Mechanics of Hydraulic Fracturing*. Houston, Texas: Gulf Publishing Company.

Lionel H. Ribeiro is a PhD candidate in the Department of Petroleum and Geosystems Engineering at the University of Texas at Austin. His current research is focused on the modeling of energized fracturing treatments with the development of the first 3D compositional fracturing simulator. Ribeiro holds a diplôme d'Ingénieur Civil des Mines from l'Ecole des Mines de Nancy in France and an MS degree in Petroleum Engineering from the University of Texas at Austin.

Mukul M. Sharma is professor and holder of the "Tex" Moncrief Chair in the Department of Petroleum and Geosystems Engineering at the University of Texas at Austin, where he has been for 27 years. He served as Chairman of the Department from 2001 to 2005. His current research interests include improved oil recovery, injection water management, hydraulic fracturing, formation damage, and petrophysics. He has published more than 200 journal articles and conference proceedings and holds 14 patents. Sharma holds a Bachelor of Technology degree in chemical engineering from the Indian Institute of Technology and MS and PhD degrees in chemical and petroleum engineering from the University of Southern California. Among his many awards, Sharma is the recipient of the 2009 SPE Anthony F. Lucas Gold Medal, the 2004 SPE Faculty Distinguished Achievement Award, the 2002 Lester C. Uren Award, and the 1998 SPE Formation Evaluation Award. He served as an SPE Distinguished Lecturer in 2002, has served on the Editorial Boards of many journals, and has taught and consulted for the industry worldwide.